vibration

MDPI

Article

A Mechanical Fault Identification Method for On-Load Tap Changers Based on Hybrid Time—Frequency Graphs of Vibration Signals and DSCNN-SVM with Small Sample Sizes

Yanhui Shi [1], Yanjun Ruan [1], Liangchuang Li [1], Bo Zhang [1], Yichao Huang [2], Mao Xia [2], Kaiwen Yuan [2], Zhao Luo [2] and Sizhao Lu [2,*]

[1] Guangzhou Bureau of EHV Power Transmission Company, China Southern Power Grid Co., Ltd., Guangzhou 510000, China; shiyanhui@ieee.org (Y.S.); ruanyanjun@ieee.org (Y.R.); liangchaungli@ieee.org (L.L.); bozhang1@ieee.org (B.Z.)

[2] Faculty of Electric Power Engineering, Kunming University of Science and Technology, Kunming 650500, China; 20232105012@stu.kust.edu.cn (Y.H.); xiamao@stu.kust.edu.cn (M.X.); 20222105010@stu.kust.edu.cn (K.Y.); waiting.1986@live.com (Z.L.)

* Correspondence: lusz10@kust.edu.cn

Abstract: In engineering applications, the accuracy of on-load tap changer (OLTC) mechanical fault identification methods based on vibration signals is constrained by the quantity and quality of the samples. Therefore, a novel small-sample-size OLTC mechanical fault identification method incorporating short-time Fourier transform (STFT), synchrosqueezed wavelet transform (SWT), a dual-stream convolutional neural network (DSCNN), and support vector machine (SVM) is proposed. Firstly, the one-dimensional time-series vibration signals are transformed using STFT and SWT to obtain time–frequency graphs. STFT time–frequency graphs capture the global features of the OLTC vibration signals, while SWT time–frequency graphs capture the local features of the OLTC vibration signals. Secondly, these time–frequency graphs are input into the CNN to extract key features. In the fusion layer, the feature vectors from the STFT and SWT graphs are combined to form a fusion vector that encompasses both global and local time–frequency features. Finally, the softmax classifier of the traditional CNN is replaced with an SVM classifier, and the fusion vector is input into this classifier. Compared to the traditional fault identification methods, the proposed method demonstrates higher identification accuracy and stronger generalization ability under the conditions of small sample sizes and noise interference.

Keywords: on-load tap changer; mechanical fault; vibration signal; small sample sizes; time–frequency graphs

check for updates

Citation: Shi, Y.; Ruan, Y.; Li, L.; Zhang, B.; Huang, Y.; Xia, M.; Yuan, K.; Luo, Z.; Lu, S. A Mechanical Fault Identification Method for On-Load Tap Changers Based on Hybrid Time—Frequency Graphs of Vibration Signals and DSCNN-SVM with Small Sample Sizes. *Vibration* **2024**, *7*, 970–986. https://doi.org/10.3390/vibration7040051

Academic Editor: Agathoklis Giaralis

Received: 15 August 2024
Revised: 13 October 2024
Accepted: 24 October 2024
Published: 28 October 2024

Copyright: © 2024 by the authors. Licensee MDPI, Basel, Switzerland. This article is an open access article distributed under the terms and conditions of the Creative Commons Attribution (CC BY) license (https://creativecommons.org/licenses/by/4.0/).

1. Introduction

The on-load tap changer (OLTC) is a critical component for voltage regulation in a transformer during operation. Its operating condition significantly impacts the operational safety of the transformer and the entire power grid [1]. Statistics indicate that transformer failures caused by the OLTC account for more than 20% of total failures, and over 70% of these OLTC failures are mechanical. If an OLTC fails to switch due to a fault, it directly affects the accuracy of the voltage ratio adjustment of the transformer, thereby compromising the stability and safety of the power system. This situation underscores the urgency of early warning and prompt handling [2,3]. Therefore, studying online monitoring methods that align with actual operating conditions is crucial to ensure the safe and stable operation of the power system.

Due to the rich equipment condition information contained in the vibration signals during the OLTC switching process, vibration analysis has gradually become a research hotspot for monitoring the mechanical conditions of OLTCs [4–6]. Reference [7] employed

variational mode decomposition (VMD) to decompose the vibration signals of an OLTC and extracted various features from each mode component to diagnose faults. Reference [8] used dynamic time warping (DTW) to calculate the distance to identify OLTC vibration signals and reference signals, thereby identifying faults. Reference [9] extracted the main components of transformer body vibration signals through cross-wavelet transform and successfully distinguished among transformer winding looseness faults, core magnetic circuit faults, and normal conditions based on these main components. Reference [10] adopted the phase space reconstruction method to convert vibration data into grayscale graphs of phase point distance mapping recurrence matrices, thereby reducing the need for experience in processing vibration data. Reference [11] generated singular phase-space values of vibration signals through Bayesian estimation phase space fusion and employed an improved support vector data description (SVDD) algorithm based on contour maps for fault identification. These methods effectively identified mechanical faults in OLTCs. However, the methods in references [4–6] involve manually designed OLTC vibration signal features, and those in references [8,9] require high expertise for OLTC vibration signal analysis. Additionally, references [10,11] indicate that the optimal parameters for phase space reconstruction vary across different conditions, and using uniform parameters may yield suboptimal results for some conditions. Therefore, there is an urgent need for a method that can effectively extract OLTC vibration signal features. There is also a need for an accurate and efficient intelligent identification model for OLTC mechanical faults to ensure the safe and reliable operation of power systems.

Time–frequency analysis is a key method for dealing with non-stationary signals. Its core principle involves converting a non-stationary signal into a joint representation of time and frequency, generating time–frequency graphs that highlight the time–frequency energy features of signals. Reference [12] constructed a local maxima estimation operator using second-order synchrosqueezing transform (SST2) to rearrange the time–frequency energy of short-time Fourier transform (STFT), achieving the fault identification of rolling bearings. Reference [13] applied STFT to the collected bearing vibration signals to obtain two-dimensional time–frequency data and then used a convolutional neural network (CNN) to extract features from the transformed data for identification. Reference [14] improved the synchrosqueezed wavelet transform (SWT) method to enhance the fault knowledge threshold, further improving identification capabilities. Since OLTC vibration signals and bearing vibration signals both belong to mechanical vibration signals, their signal analysis methods can be mutually referenced.

In recent years, deep learning has driven advancements across various fields. CNNs have been widely used in detecting railway defects, monitoring volcanic eruption activities, and in the medical field [15–17]. Reference [18] employed the Gramian angular summation field (GASF) to transform multi-sensor signals into 2D feature maps and utilized a deep belief network (DBN) to construct a robust deep learning framework for effective bearing fault identification. CNNs are favored for their low computational complexity, strong robustness, and high fault tolerance. They can automatically extract features from data, reducing dependence on expert prior knowledge. CNNs possess excellent self-learning and automatic feature extraction capabilities, allowing graphs to be directly input into the network. This approach avoids the complex feature pre-extraction and data reconstruction processes required by traditional machine learning algorithms and neural networks [19]. Deep learning network models, such as CNN and ResNet, simulate the human brain structure and self-learning capabilities, relying on large datasets for training to classify OLTC mechanical faults. However, these models perform poorly in small-sample-size scenarios. In reference [20], transfer learning was employed to apply the knowledge learned from large datasets to the target domain with small samples, enabling small-sample-size fault identification. However, the distribution differences between the source and the target domains were difficult to quantify, leading to the risk of negative transfer. References [21,22] used generative models to expand the sample sizes, but it was challenging to assess the accuracy and diversity of the generated samples. Reference [23] introduced the minimum

sigma set and scaled unscented transform, improving the ability to discriminate fault features in low-speed imbalanced data and enhancing the efficiency of the identification model. However, in real-world applications, the imbalance ratio may fluctuate, reducing the effectiveness of this solution under varying conditions. Reference [24] introduced a multi-agent reinforcement learning method for rotating machinery fault identification, improving small-sample-size fault identification accuracy through a novel reward mechanism. However, the model heavily relies on reward function design and delays the feedback in complex scenarios, which limits further optimization of the model. Reference [25] presents a small-sample-size fault identification method for rolling bearings based on continuous wavelet transform (CWT) and a Siamese neural network (SNN). Despite its improved accuracy, it demands high time and frequency resolution, potentially lowering the performance for noisy or complex signals. Reference [26] proposed a lightweight UNet (LWUNet) model with wavelet packet decomposition (WPD) and attention fusion residual blocks (AFRBs) for small-sample-size fault identification of rolling bearings. While effective, it may face performance bottlenecks with high-dimensional signals, and its demands on computing resources increase. In contrast, SVM classifiers excel in classification problems with fewer training samples but have weaker feature extraction capabilities. Reference [27] proposed using an improved CNN to extract features from brake friction signals and employing a support vector machine (SVM) to classify these features, achieving the precise detection of brake faults. This validated the feasibility of the CNN+SVM basic model. Combining the feature extraction ability of CNNs with the small-sample-size classification capability of SVMs is expected to achieve the accurate identification of OLTC mechanical faults.

In summary, the following issues still exist in the field of OLTC mechanical fault identification:

(1) There is noise in the actual sampled signals, and there is a lack of methods to effectively extract OLTC vibration signal features under noisy conditions.
(2) Most of the aforementioned identification methods rely on large datasets. However, OLTCs are in a normal state most of the time, and the number of samples with abnormal conditions is low. There is a lack of effective methods for identifying mechanical faults in OLTC with small sample sizes.

Based on the above analysis, this paper proposes a small-sample-size OLTC fault identification method utilizing STFT, SWT, a dual-stream CNN (DSCNN), and SVM. The proposed method employs time–frequency graphs from STFT and SWT as inputs and replaces the softmax classifier in the traditional CNN model with an SVM classifier to construct a DSCNN-SVM classification model, which is more suitable for small-sample-size OLTC mechanical fault identification scenarios. The proposed method then analyzes the time–frequency graphs of vibration signals during the switching process under normal and typical mechanical fault conditions of a UCG-type OLTC and compares the effects of different imaging methods and hybrid time–frequency graphs on the classification results. With only 20 training samples per fault type and under noise pollution at 10 dB, the fault identification accuracy of the proposed method can still reach 95% or above.

The contributions of this paper are listed as follows:

(1) A hybrid time–frequency feature extraction method is proposed to overcome the drawbacks of low fault identification accuracy caused by the insufficient information in single time–frequency graphs. This approach uses a dual-channel CNN to extract the STFT feature vectors and SWT feature vectors of OLTC vibration signals separately. In the fusion layer, the feature vectors extracted by the dual-channel CNN are fused, resulting in significantly enhanced time–frequency features that encompass both the local and global features of the OLTC vibration signal time–frequency graphs.
(2) An SVM classifier is employed to replace the softmax classifier in the traditional CNN model, constructing a DSCNN-SVM classification model that is more suitable for small-sample-size OLTC mechanical fault identification. This approach effectively overcomes the issue of deep learning models being highly sensitive to the number of samples.

(3) A small-sample-size fault identification model based on hybrid time–frequency graphs and DSCNN-SVM is established, and this model is applied to the fault identification of UCG-type OLTC, achieving good identification results.

2. Basic Principles of STFT and SWT

2.1. STFT

To fully leverage the capabilities of a CNN, it is necessary to convert one-dimensional time-series signals into a two-dimensional matrix format that the CNN can process effectively. STFT is used to transform time-domain signals into feature spectrums containing both time-domain and frequency-domain information [28]. The fundamental concept of STFT involves using a fixed-length window function to segment the global signal into multiple independent time-domain segments. Each segment is then subjected to Fourier transform to obtain the local spectrum within a small time frame. This spectral information is arranged chronologically, resulting in time–frequency spectrum information that depicts the variation in the different frequency components of the original signal over time.

The expression of the input OLTC vibration signal $x(t)$ after undergoing STFT transformation can be defined as

$$\mathrm{STFT}\{x(t)\}(t,\omega) = \int_{-\infty}^{+\infty} x(t)h(t-\omega)\mathrm{e}^{-\mathrm{j}\omega t}\mathrm{d}t \tag{1}$$

where $\mathrm{STFT}\{x(t)\}(t,\omega)$ represents the output of the STFT, and $h(t-\omega)$ is the window function.

For STFT, the selection of the window function significantly affects the calculation results. The choice involves both the type of window function and its width. Selecting an appropriate window length can better handle and analyze the original signal. Commonly used window functions include rectangular, triangular, and Hanning windows. To avoid boundary effects, this paper selected the Hanning window for its smooth boundaries.

2.2. SWT

A limitation of STFT is that its window function lacks adaptability, whereas the time–frequency resolution of SWT varies with the scale parameter. OLTC vibration signals are typical non-stationary signals, with signal components exhibiting quasi-stationary features at low frequencies and transient amplitude changes at high frequencies. The properties of SWT make it particularly suitable for analyzing OLTC vibration signals. The SWT algorithm can be divided into three steps, detailed as follows:

(1) Assume that the OLTC vibration signal $f(t)$ undergoes continuous wavelet transform (CWT) to yield the following:

$$\mathrm{WT}(a,b) = \frac{1}{\sqrt{a}}\int_{-\infty}^{+\infty} f(t)\widetilde{\psi}\left(\frac{t-b}{a}\right)dt \tag{2}$$

where a is the scale factor, b is the translation factor, $\psi(t)$ is the wavelet basis function, and $\widetilde{\psi}(t)$ is the conjugate function of $\psi(t)$.

According to Parseval's theorem, the process of transforming $\mathrm{WT}(a,b)$ into the frequency domain is as follows:

$$\mathrm{WT}_f(a,b) = \frac{1}{2\pi}\int \hat{f}(\omega)\hat{\psi}(\omega)\mathrm{e}^{\mathrm{j}b\omega}a^{1/2}\mathrm{d}\omega \tag{3}$$

where $\hat{f}(\omega)$ and $\hat{\psi}(\omega)$ are the Fourier transforms of $f(\omega)$ and $\psi(\omega)$ respectively, ω represents frequency, and j denotes the imaginary unit.

(2) Calculate the instantaneous frequency of the signal. If the wavelet basis function is concentrated around the center frequency ω_0, then the wavelet coefficients are distributed around the scale $a = \omega_0/\omega$, causing the time–frequency signal curve to

become blurred, especially when the signal exhibits chaotic features. Although the wavelet coefficients exhibit dispersion in the frequency direction, the phase of the signal remains unchanged. Therefore, according to Equation (3), by solving for the phase of the wavelet coefficients in the time domain, the instantaneous frequency $\omega_f(a,b)$ of the signal can be obtained as follows:

$$\omega_f(a,b) = -\mathrm{j}\frac{\frac{\partial}{\partial b}\mathrm{WT}_f(a,b)}{\mathrm{WT}_f(a,b)} \tag{4}$$

(3) Compress and reorganize the equation to obtain synchrosqueezed wavelet transform values. Using Equation (4), wavelet coefficients are transformed from the time domain to the time–frequency domain, followed by frequency compression and reconstruction to concentrate the energy, thereby improving the blurring phenomenon in the frequency domain. By compressing and rearranging the wavelet coefficients, the formula for synchrosqueezed wavelet transform $\mathrm{SWT}_f(b,\omega)$ is obtained as follows:

$$\mathrm{SWT}_f(b,\omega) = \int WT_f(a,b)a^{-3/2}\delta[\omega(a,b)-\omega]da \tag{5}$$

where $\delta(\cdot)$ is the Dirac delta function.

3. A Small-Sample-Size OLTC Fault Detection Method Based on Hybrid Time–Frequency Graphs and DSCNN-SVM

3.1. Fundamental Structure of CNN

The powerful feature extraction capability of a CNN makes it suitable for handling matrix data. A traditional CNN includes an input layer, convolutional layers, pooling layers, and fully connected layers [29]. Its structure is illustrated in Figure 1.

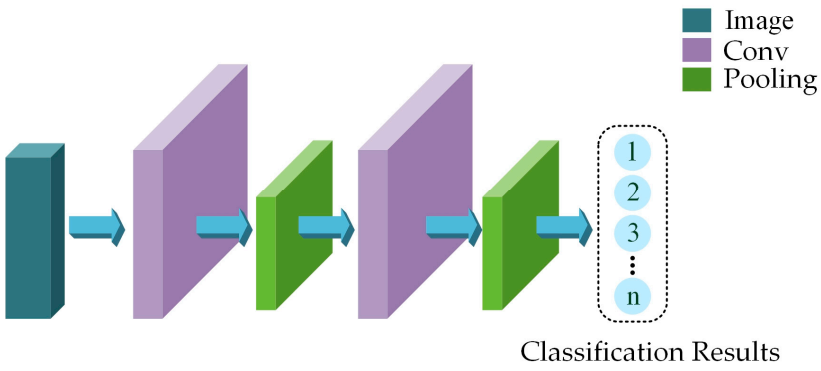

Figure 1. Structure of CNN.

In CNN data processing, the convolutional layer uses convolutional kernels to perform convolution operations on the input samples, followed by nonlinear transformation through an activation function to generate feature parameters. These parameters are used to capture local features in the input data and extract higher-level details in subsequent layers. The output feature of the i-th layer in CNN is represented as $\mathbf{Z}_i$, and the operation of the convolutional layer can be expressed as follows:

$$\mathbf{Z}_i = \sigma(\mathbf{Z}_{i-1} \otimes \mathbf{F}_i + \mathbf{b}_i) \tag{6}$$

where $\otimes$ represents the convolution operation, $\mathbf{F}_i$ denotes the weight matrix of the convolutional kernel used in the i-th layer, $\mathbf{b}_i$ represents the bias vector of the i-th layer, and $\sigma(\cdot)$ denotes the activation function.

The pooling layer aggregates feature parameters within a certain range of the convolutional layer output into a single feature, thereby reducing the data processing volume while retaining useful information. The calculation process is as follows:

$$\mathbf{Z}_i = \text{pooling}(\mathbf{Z}_{i-1}) \tag{7}$$

where pooling$(\cdot)$ represents the pooling operation.

The fully connected layer performs a weighted summation of the data output from the pooling layer, followed by nonlinear transformation through an activation function. The calculation process can be expressed as follows:

$$\mathbf{Z}_i = \sigma(w_i \mathbf{Z}_{i-1} + b_i) \tag{8}$$

where w_i represents the weights of the fully connected layer.

When using CNN to handle classification problems, the output layer typically consists of a fully connected layer and a softmax classifier. The softmax classifier performs probability normalization on the final classification results. However, its performance is easily affected by the number of samples and the distribution of categories. When the sample size is insufficient, the model training lacks generalization, leading to classification results that tend to concentrate on categories with a larger number of samples.

3.2. Operating Principle and Structure of SVM

SVM is an algorithm based on applied statistical learning theory that performs well in small-sample-size classification problems [30]. The main idea is to map the data into a high-dimensional space and construct an optimal separating hyperplane to distinguish between linearly and non-linearly inseparable samples in the input space. The class imbalance and balanced situations for SVM classification principles are shown in the classification principle in Figure 2.

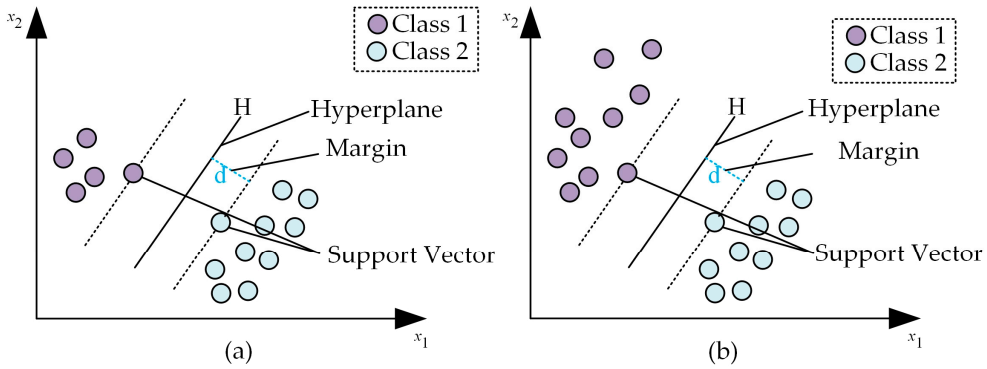

Figure 2. SVM classification principles: (**a**) imbalanced classes; (**b**) balanced classes.

As observed in Figure 2a, when there are more samples in Class 2, the selection of the optimal hyperplane by the algorithm is determined by the support vectors that are closest to the hyperplane from both classes. The principle for selecting the support vectors is based on the samples that are "closest" in the high-dimensional space. The support vectors in Class 1 will not be mistakenly selected due to the smaller number of samples. As observed in Figure 2b, when the numbers of samples in Class 1 and Class 2 are balanced, the selection of the optimal hyperplane by the algorithm is still determined by the support vectors that are closest to the hyperplane from both classes. The impact of sample imbalance on the model training results is primarily reflected in the insufficient training of the minority class samples. However, theoretically, the SVM classification algorithm can effectively handle the challenge of small sample training; therefore, it has certain advantages in dealing with the problem of sample imbalance.

In summary, the determination of the SVM hyperplane is primarily influenced by a few support vectors and is not affected by the number of samples. Therefore, SVM is more suitable for small-sample classification. However, due to the minimal differences between OLTC vibration signals of different fault types and normal conditions and the limited ability of SVM to distinguish deep features among different operating conditions, its application in OLTC fault identification is restricted.

3.3. DSCNN-SVM Fault Identification Model

To address the limitations of the traditional CNN and SVM models, this paper proposes an improved DSCNN-SVM fault identification model. This model combines the powerful feature extraction capability of CNN with the advantages of SVM in small-sample-size classification problems, accurately identifying OLTC mechanical faults. The improvements are as follows: a dual-channel CNN is constructed to extract features from STFT and SWT time–frequency graphs, respectively. Meanwhile, an SVM classifier designed for eight-class classification replaces the softmax classifier in the CNN model, improving the accuracy of OLTC mechanical fault identification. The DSCNN-SVM fault identification model is illustrated in Figure 3.

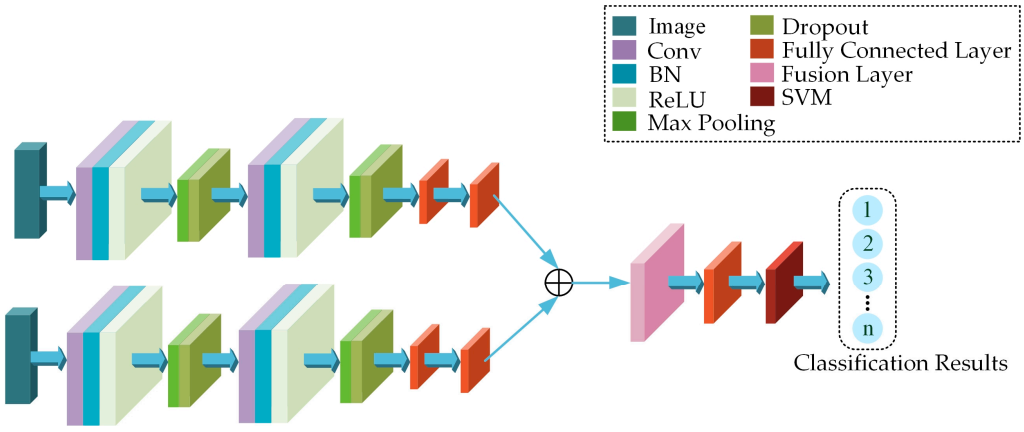

Figure 3. DSCNN-SVM structure.

In the improved DSCNN-SVM fault identification model, the STFT and SWT time–frequency graphs of the OLTC vibration signals are first input into the model. They undergo convolution (Conv), batch normalization (BN), rectified linear unit (ReLU) activation function, max pooling and dropout operations. These operations are repeated twice, followed by a fully connected layer. Next, the feature quantities of the STFT and SWT channels are fused. Finally, the fused features from the dual channels and their corresponding labels are input into the SVM classifier for fault identification.

The DSCNN-SVM fault identification model improves its generalization ability through various techniques to prevent overfitting. These techniques include using dropout layers to randomly ignore some neurons, batch normalization to stabilize the training process, L2 regularization to limit the complexity of the model, mini-batch training to avoid data dependency, and shuffling the data in each iteration to reduce sequence dependence. These methods effectively reduce the risk of overfitting in the proposed model.

3.4. OLTC Mechanical Fault Identification Process Based on DSCNN-SVM Model

To improve the accuracy of OLTC mechanical fault identification, this paper proposes a small-sample-size fault identification combination model based on STFT, SWT, DSCNN, and SVM. The detailed structure of the model is illustrated in Figure 4. This combined model includes a signal preprocessing section and a feature extraction and identification section.

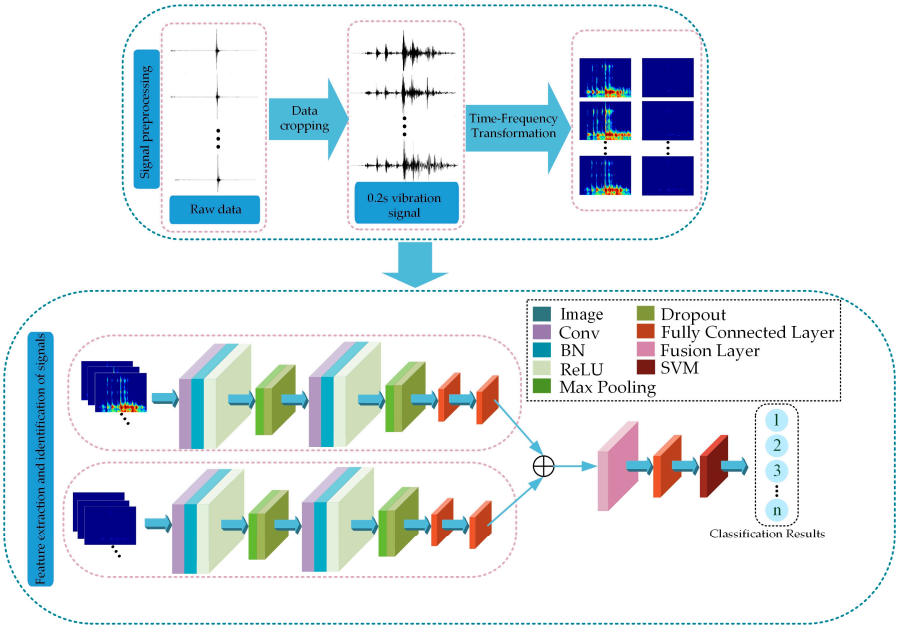

Figure 4. Identification process.

(1) Signal preprocessing. This method uses STFT and SWT to perform time–frequency transformation on OLTC vibration signals, obtaining STFT time–frequency graphs and SWT time–frequency graphs, and thus achieving time–frequency analysis of non-stationary signals. Using these two types of time–frequency graphs as feature inputs provides more dimensional information for fault signal classification. the SWT captures the local features of the OLTC vibration signals, while the STFT extracts the global features, effectively reflecting the inherent patterns among the different fault signal categories.

(2) Feature extraction and identification. First, the STFT and SWT time–frequency graphs are input into the DSCNN. One CNN branch extracts the global features of the OLTC vibration signals, while the other branch captures local features, thereby extracting key features from the input time–frequency graphs. Next, in the fusion layer, the STFT feature vectors and SWT feature vectors extracted by the dual-channel CNN are fused to obtain significantly enhanced features that achieve complementary detail representation. Finally, after passing through the fully connected layer, the SVM classifier is used to classify the fault types, addressing the issue of low identification accuracy in deep learning models with small sample sizes, and accomplishing the identification of OLTC mechanical faults.

4. Experimental Verification

4.1. Data Description

An experimental testing setup was built at the transformer factory, where four AD100T vibration sensors (Shenzhen Vkinging Electronics Co., Ltd., Shenzhen, China) and a VK702NH-Pro data acquisition card (Shenzhen Vkinging Electronics Co., Ltd., Shenzhen, China) were employed. The vibration sensor had a response frequency of 0.3 to 15,000 Hz, and the data acquisition card had a sampling frequency of 50 kHz. The experimental testing setup is shown in Figure 5. Figure 6a shows the pictures of the vibration sensor installation. Four AD100T vibration sensors, with a sensitivity of 100 mV/g, a range of ±50 g, and a frequency range of 2–20 kHz, were installed on the top of a UCG-type OLTC to acquire the vibration signals generated during the switching process of the OLTC under different fault conditions.

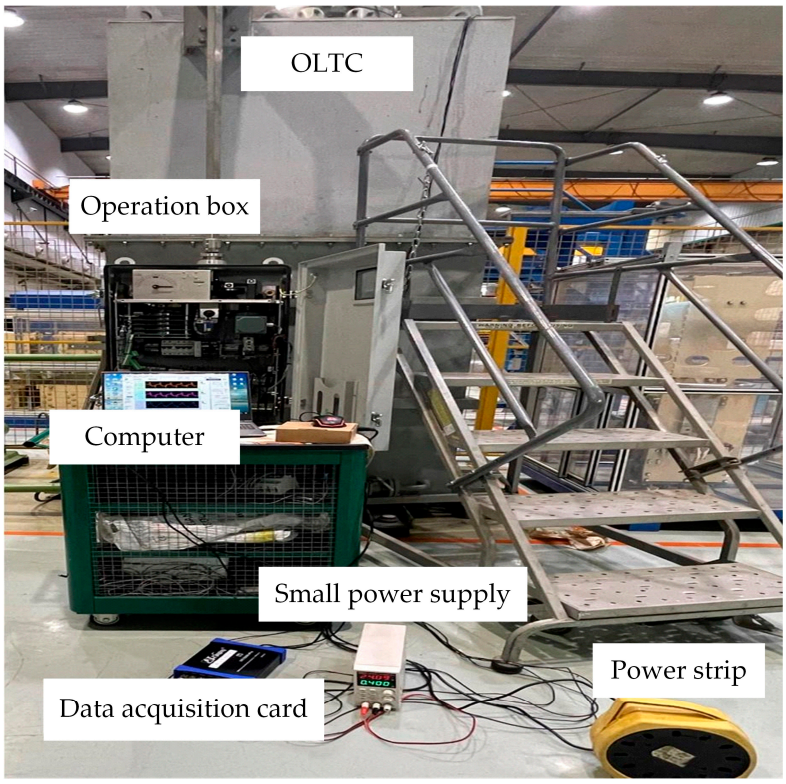

Figure 5. Picture of the experimental testing setup.

Eight types of fault conditions were set, including normal conditions, upper static contact looseness, lower static contact looseness, insulated panel looseness, moving contact looseness, contact erosion, contact wear, and jamming. For each operating condition, 720 samples were collected, with each sample having an acquisition time of 7 s. Since the actual operation time of OLTC was less than 0.2 s, a vibration signal of 0.2 s was enough to retain its effective information. Therefore, the vibration signals were trimmed to 0.2 s to reduce the data sizes and processing times.

Figure 6b–h represent the upper static contact looseness, lower static contact looseness, insulated panel looseness, moving contact looseness, contact erosion, wear, and jamming, respectively. As shown in Figure 6b, the jamming fault was simulated by continuously adding wood chips. As shown in Figure 6c, the fault of the insulation plate looseness was set by loosening the screws of the insulation plate. As shown in Figure 6d, the fault of the lower stationary contact looseness was set by loosening the screws of the lower stationary contact. As shown in Figure 6e, the fault of the upper stationary contact looseness was set by loosening the screws of the upper stationary contact. As shown in Figure 6f, the fault of the moving contact looseness was simulated by cutting the spring that connected the moving contact. As shown in Figure 6g, the contact erosion fault was set by partially roughening the surface of the contact using an electric drill. As shown in Figure 6h, the contact wear fault was set by partially wearing down the contact.

The UCG-type OLTC vibration signals under different operating conditions are shown in Figure 7. By comparing Figure 7c,e,g,i,k,m,o with Figure 7a, it can be observed that when different types of looseness faults occurred, the vibration signal intensity in the time domain changed, and the waveform showed significant differences. A comparison of Figure 7d,f,h,i,l,n,p with Figure 7b reveals that in the frequency domain, when the jamming fault, insulated panel looseness, lower static contact looseness, upper static contact looseness, and contact wear occurred, a significant number of low-frequency components appeared in the vibration signal. When contact erosion occurred, both the high-frequency and low-frequency components of the vibration signal decreased. Therefore, the mechanical

fault identifications of the OLTC can be achieved by extracting the time–frequency features of the OLTC vibration signals.

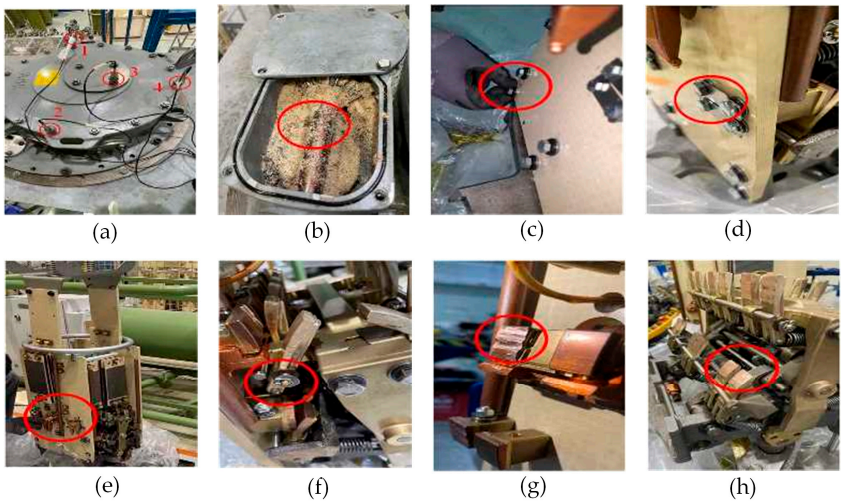

Figure 6. Sensor installation and fault condition setting: (**a**) sensor installation; (**b**) jamming; (**c**) insulated panel looseness; (**d**) lower static contact looseness; (**e**) upper static contact looseness; (**f**) moving contact looseness; (**g**) contact erosion; (**h**) contact wear.

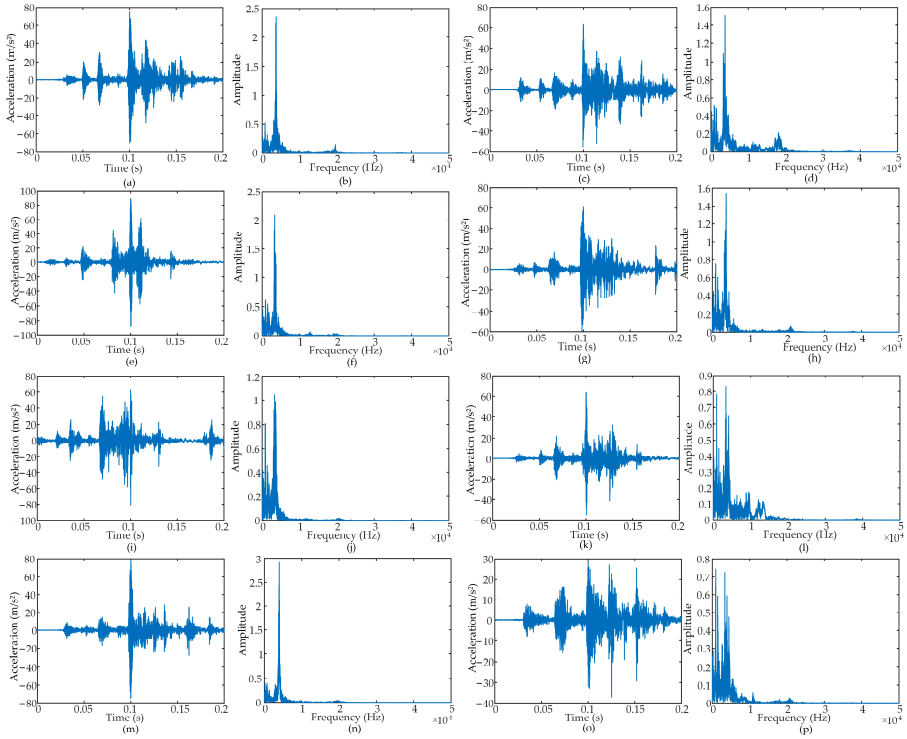

Figure 7. UCG-type OLTC vibration signals under different operating conditions: (**a**) normal condition time-domain signal; (**b**) normal condition frequency-domain signal; (**c**) jamming time-domain signal; (**d**) jamming frequency-domain signal; (**e**) insulated panel looseness time-domain signal; (**f**) insulated panel frequency-domain signal; (**g**) lower static contact looseness time-domain signal; (**h**) lower static contact looseness frequency-domain signal; (**i**) upper static contact looseness time-domain signal; (**j**) upper static contact looseness frequency-domain signal; (**k**) moving contact looseness time-domain signal; (**l**) moving contact looseness frequency-domain signal; (**m**) contact erosion time-domain signal; (**n**) contact erosion frequency-domain signal; (**o**) contact wear time-domain signal;. (**p**) contact wear frequency-domain signal.

For each type of fault, a maximum of 50 samples were selected for the training set, 100 samples for the validation set, and 100 samples for the test set to evaluate the effectiveness of the proposed model for identifying faults with small sample sizes.

4.2. Data Preprocessing

As an example of data collected from the test setup, the vibration signals were converted from one-dimensional time-domain signals into two-dimensional time–frequency graphs using STFT and SWT. The number of sampling points was set to 20,000, and the resolution was 64 × 64. The energy axis of the time–frequency graphs was normalized, and the calculation process was as follows:

$$T_{\text{norm}}(i,j) = \frac{|T(i,j)|}{\max(|T|)} \tag{9}$$

where $|T(i,j)|$ is the absolute value of the element at the i-th row and j-th column in the original time–frequency matrix T, $\max(|T|)$ denotes the maximum absolute value among all elements in matrix T, $T_{\text{norm}}(i,j)$ is the normalized value of the element in the matrix at the i-th row and j-th column, and its range is [0, 1].

For each type of OLTC fault category, one graph sample was selected for display. The time–frequency graphs obtained from SWT and STFT are shown in Figures 8 and 9, respectively.

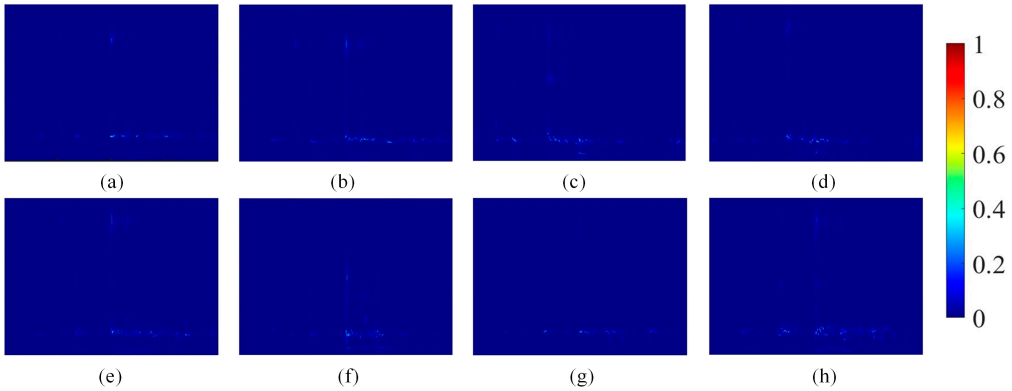

Figure 8. SWT time–frequency graphs: (**a**) normal; (**b**) jamming; (**c**) insulated panel looseness; (**d**) lower static contact looseness; (**e**) upper static contact looseness; (**f**) moving contact looseness; (**g**) contact erosion; (**h**) contact wear.

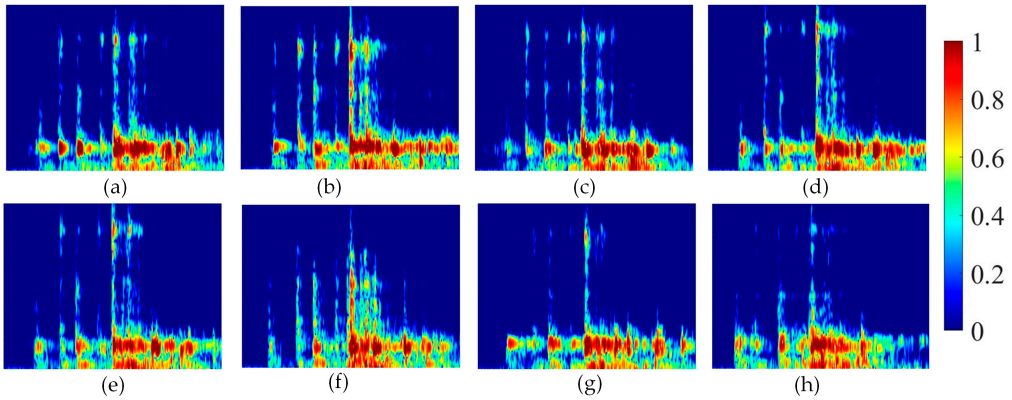

Figure 9. STFT time–frequency graphs: (**a**) Normal; (**b**) Jamming; (**c**) Insulated panel looseness; (**d**) Lower static contact looseness; (**e**) Upper static contact looseness; (**f**) Moving contact looseness; (**g**) Contact erosion; (**h**) Contact wear.

In Figure 8, it can be seen that SWT, with its multi-scale analysis capability and adaptive time–frequency distribution features, could more comprehensively capture the local features of OLTC vibration signals, avoiding the problem of the signal frequency being ignored or distorted. The texture shapes and distribution differences of the various operating conditions on the SWT time–frequency graphs are distinct, reflecting different fault types. In Figure 9, it can be observed that STFT analyzed the signal using a fixed window function, corresponding to the frequency features of the signal. Therefore, the STFT time–frequency graphs focused more on the global features of OLTC vibration signals, showcasing the abundant time–frequency energy features of various OLTC vibration signals.

The complementarity of global and local features in time–frequency domain analysis methods is often overlooked. Effectively linking this complementarity can better capture the time–frequency features of OLTC vibration signals. The pixel differences between the two types of time–frequency graphs for different fault types are considerable; the SWT time–frequency graphs focus more on local details, while the STFT time–frequency graphs highlight the global features. Using these as inputs for the DSCNN-SVM can further enhance the feature extraction capabilities of the model and improve classification accuracy.

4.3. Comparison of Different Imaging Methods

The traditional methods for converting one-dimensional time-series signals into two-dimensional graphs include continuous wavelet transform (CWT), Gramian angular fields (GAFs), Markov transition fields (MTFs), and recurrence plots (RPs).

To verify the identification effects of different imaging methods, a dataset was constructed at a 20 dB noise level, with 20 samples for each OLTC fault type in the training set and 100 samples in the test set. The CNN built in MATLAB was used for training, with the optimizer set to Adam, the learning rate set to 0.001, and a total of 240 iterations. To reduce experimental randomness, an average accuracy of 10 test set simulations was selected as the final identification accuracy of the model. The test set accuracy is shown in Figure 10.

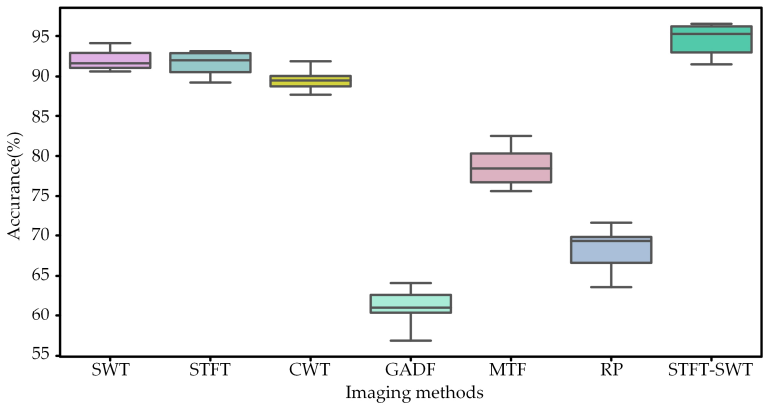

Figure 10. Comparison of different imaging methods.

According to the experimental results shown in Figure 10, SWT and STFT achieved higher accuracy. Specifically, the accuracy of SWT ranged from 90.62% to 94.12%, with an average of 91.89%. The accuracy of STFT ranged from 89.25% to 93.12%, with an average of 91.59%. In comparison, the other imaging methods had relatively lower accuracy: CWT ranged from 87.75% to 91.88%, and the performances of GADF, GASF, MTF, and RP were significantly worse. Therefore, this paper proposed a hybrid time–frequency method that uses STFT and SWT time–frequency graphs as input. The STFT-SWT method achieved the highest accuracy, with an average accuracy of 94.61%. This indicates that the dual-channel effect constructed by the STFT-SWT imaging method is at least as good as the single-channel methods. Considering that STFT-SWT incorporates more temporal and spatial features, it was ultimately selected as the optimal graph generation method.

4.4. Comparison of Different Identification Methods

In actual engineering operations, the working environments of OLTCs are complex and variable, and the insufficient number of samples affects the final fault identification accuracy. We used the proposed DSCNN-SVM fault diagnosis model to conduct generalization performance experiments under different noise levels. For each type of fault, 20, 30, 40, and 50 training samples were selected to verify the model's fault identification capability under small-sample-size conditions.

To validate the effectiveness of the proposed method for OLTC fault identification, the DSCNN-SVM model was compared with STFT-CNN, SWT-CNN, STFT-CNN-SVM, SWT-CNN-SVM, and DSCNN models. Among these, STFT-CNN, SWT-CNN, STFT-CNN-SVM, and SWT-CNN-SVM are single-channel models, while DSCNN-SVM and DSCNN are dual-channel models. Figure 11 shows the average loss and accuracy on the validation set over five experiments, with 20 samples per fault type and at a 20 dB noise level. In the early iterations, the loss and accuracy on the validation set fluctuated slightly for all methods. After 100 iterations, the DSCNN-SVM achieved low loss values and stable high accuracy on the validation set, significantly outperforming the other five methods. However, the accuracy of single-channel networks on the validation set after convergence was notably lower than that of the dual-channel networks. This is because the four single-channel models using only one type of time–frequency graphs strategy resulted in the loss of certain features in the vibration signal, while the dual-channel networks captured both the local and global features of the time–frequency graphs, thereby learning the multidimensional information contained in the signals. Additionally, during repeated training, DSCNN-SVM achieved lower loss values and higher accuracy compared to DSCNN, with very fast convergence times, indicating the effectiveness of the SVM classifier in replacing the softmax classifier in CNN models for small sample sizes.

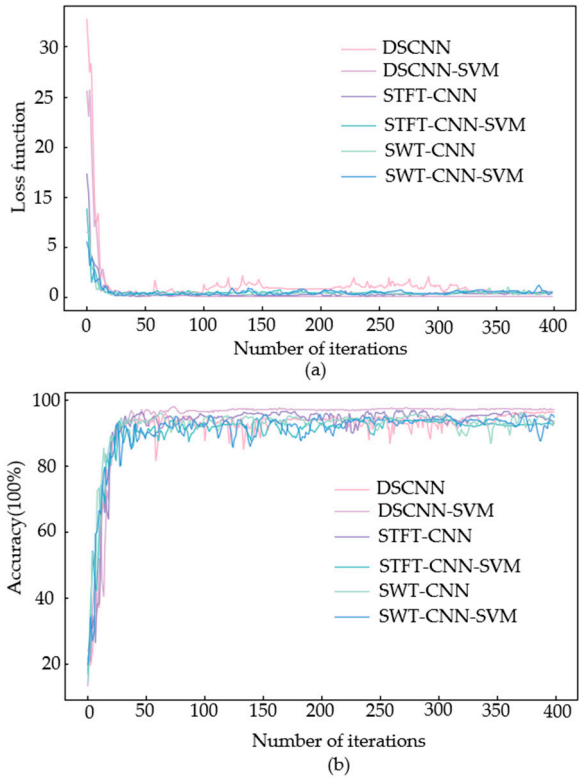

Figure 11. Comparison of validation accuracy and loss function for different methods: (**a**) loss function curve; (**b**) accuracy curve.

Table 1 shows the average identification accuracy of each method on the test set over 10 experiments under different noise levels and sample sizes. From Table 1, the following

conclusions can be drawn: (1) DSCNN-SVM achieved higher classification accuracy in all experiments compared to the other five methods. (2) Replacing the softmax classifier in the CNN model with an SVM classifier resulted in higher accuracy across all experiments, demonstrating that the SVM classification algorithm can theoretically overcome the challenges of small-sample-size training. (3) When the number of training samples per fault type was 20 and the noise level was 10 dB, the average fault identification accuracy of DSCNN-SVM was 95.56%, which was 4.59% higher than that of DSCNN and 8.45% higher than the worst-performing STFT-CNN. (4) At a noise level of 10 dB and training sample sizes of 30, 40, and 50 per fault type, the fault identification accuracy rates of DSCNN-SVM were 97.79%, 98.02%, and 99.31%, respectively, which were improvements of 0.1% to 5.45% over the other models. (5) It is evident that the accuracy rates of DSCNN and DSCNN-SVM were significantly higher than that of the single-channel time–frequency graphs. (6) Although traditional deep learning models, such as STFT-CNN, SWT-CNN, STFT-CNN-SVM, and SWT-CNN-SVM, have shorter identification times, multiple experiments have shown that their accuracy and robustness are insufficient. From the perspective of the identification results, the DSCNN-SVM model overcame these drawbacks. The identification time of the proposed model was less than 1 s. Compared to the traditional DSCNN model, although the identification time increased by about 0.3 s, the accuracy and robustness of the proposed model were significantly improved.

Table 1. Comparison of model accuracy rates and operating durations under different signal-to-noise ratios and sample sizes.

Number of Samples	Methods	Accuracy (100%)					Operating Duration	
		Normal	40 dB	30 dB	20 dB	10 dB	Iteration Once (ms)	Testing Time(s)
20	STFT-CNN	93.26	93.58	91.83	91.59	87.11	99.35	0.1
	SWT-CNN	91.5	91.31	91.51	91.08	90.29	94.5	0.09
	STFT-CNN-SVM	94.41	93.9	93.2	92.46	88.41	93.55	0.08
	SWT-CNN-SVM	92.19	92.29	91.83	91.66	90.38	92.35	0.09
	DSCNN	94.61	95.29	97.39	93.26	90.97	472.05	0.38
	DSCNN-SVM	98.85	97.36	98.28	96.77	95.56	471.6	0.7
30	STFT-CNN	94.93	95.27	95.31	94.24	92.34	109.4	0.08
	SWT-CNN	95.45	95.3	95.25	94.29	92.17	107.65	0.07
	STFT-CNN-SVM	95.24	95.41	95.52	94.98	92.98	103.75	0.08
	SWT-CNN-SVM	95.48	95.33	95.47	95.44	94.09	101.65	0.09
	DSCNN	98.24	98.15	97.7	98.11	97.09	541.65	0.31
	DSCNN-SVM	98.99	98.81	99.16	98.68	97.79	538	0.78
40	STFT-CNN	96.8	96.15	96.46	96.05	94.94	123.8	0.12
	SWT-CNN	96.87	97.1	96.77	96.84	96.35	119.05	0.08
	STFT-CNN-SVM	96.81	96.8	96.5	96.05	95.49	117.9	0.09
	SWT-CNN-SVM	97.24	97.47	97.21	96.92	96.55	117.1	0.08
	DSCNN	98.54	98.82	98.66	98.26	97.4	588.6	0.31
	DSCNN-SVM	99.55	99.23	99.2	98.42	98.02	582.15	0.72
50	STFT-CNN	96.6	96.67	96.61	95.89	95.45	135.8	0.09
	SWT-CNN	97.39	97.41	96.81	97.57	97.04	135.05	0.09
	STFT-CNN-SVM	96.98	96.85	96.73	96.64	95.59	128.4	0.08
	SWT-CNN-SVM	97.76	97.91	97.45	97.6	97.39	130.7	0.08
	DSCNN	98.96	98.33	99.36	98.23	99.24	596.2	0.32
	DSCNN-SVM	99.21	99.52	99.4	99.12	99.31	632.55	0.71

The hybrid time–frequency feature extraction method proposed in this paper effectively integrates the local features of OLTC vibration signals extracted by SWT with the global features of OLTC vibration signals obtained by STFT. This method is capable of extracting OLTC vibration signal features effectively even under noisy conditions. Consequently, the proposed method performed well even under noisy conditions. Figure 12

shows the time–frequency graphs of OLTC vibration signals under different noise levels. By comparing Figure 12a,b, when the noise level increased to 10 dB, the energy generated by the noise in Figure 12b overwhelmed much of the energy from the OLTC vibration signal, but the overall features of the OLTC vibration signal were retained. Similarly, by comparing Figure 12c,d, even when the noise level increased to 10 dB, the impact of the noise energy on the OLTC vibration signal energy in Figure 12d was minimal. Therefore, by utilizing the complementary features of these two time–frequency graphs extracted by SWT and STFT as input features, the proposed model performed well even under noisy conditions.

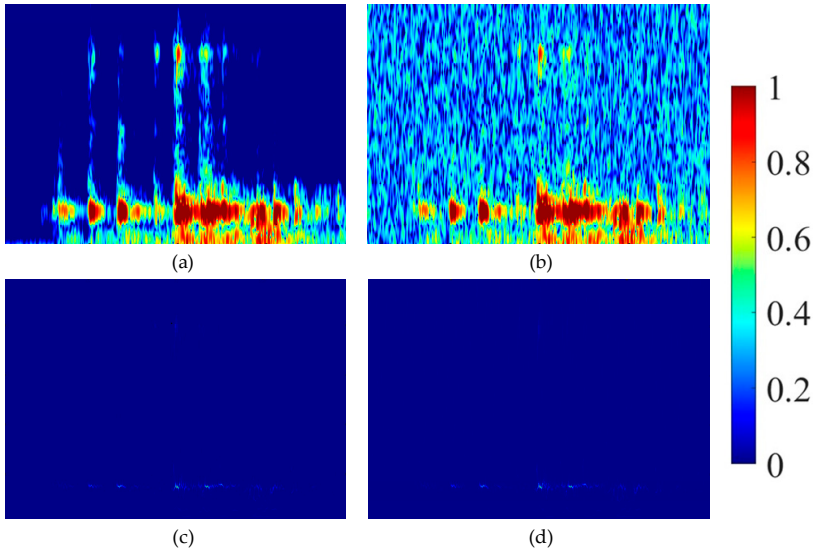

Figure 12. Time–frequency graphs of OLTC vibration signals under different noise levels: (**a**) STFT time–frequency graphs without noise; (**b**) STFT time–frequency graphs with 10 db noise; (**c**) SWT time–frequency graphs without noise; (**d**) SWT time–frequency graphs with 10 db noise.

This indicates that under the conditions of small sample sizes and high noise, DSCNN-SVM still maintained high fault identification accuracy, reflecting its stronger feature extraction capability and generalization performance.

5. Conclusions

To address the issues of insufficient OLTC vibration signal training samples, complex operating conditions leading to difficulties in feature extraction, and inconsistent data distribution, a small-sample-size OLTC mechanical fault identification method based on STFT, SWT, DSCNN, and SVM is proposed. Data were obtained through an OLTC experimental testing setup, and the obtained data were used for the training and testing of the proposed method. The testing results show the advantages of the proposed method compared to other methods. Based on the analysis in this paper, the following conclusions are drawn for the fault identification model based on DSCNN-SVM:

(1) From the perspective of vibration signal processing, this paper utilized the multiscale analysis capability and adaptive time–frequency distribution of SWT to comprehensively capture the local time–frequency features of OLTC vibration signals. STFT with a fixed window function was used to analyze the signals, so that its frequency features corresponded to those of the signal, and the global time–frequency features of the OLTC vibration signals were obtained. By combining the time–frequency graphs of STFT and SWT, the time–frequency features of the OLTC vibration signals were maximally preserved.

(2) From the perspective of network identification, this paper proposes a DSCNN-SVM model. The model uses a dual-channel CNN to separately extract the STFT feature vectors and SWT feature vectors of OLTC vibration signals. In the fusion layer, the

feature vectors extracted by the dual-channel CNN are fused to obtain significantly enhanced time–frequency features, which include both the local and global time–frequency graphs features of the OLTC vibration signals, and the softmax classifier in the CNN model is replaced with an eight-class SVM classifier for OLTC mechanical fault identification. Compared to traditional CNN models, the DSCNN-SVM model performed exceptionally well in small-sample-size classification and is more suitable for OLTC mechanical fault identification.

(3) The DSCNN-SVM model used in this study, validated using data from the OLTC experimental testing setup, achieved a fault identification accuracy of approximately 95% even with only 20 samples per fault type in the training set and under noise pollution at a 10 dB level. This further demonstrates the generalization and robustness advantages of the proposed model.

(4) In this manuscript, only a single fault scenario was considered. A fault scenario with multiple faults is a good research direction for our future research.

(5) This manuscript not only proposes that the hybrid time–frequency graphs and DSCNN-SVM network are applicable to the field of OLTC fault identification but also that the feature extraction methods and models can also be extended to other types of mechanical systems, integrating more advanced noise reduction techniques or exploring real-time applications in industrial settings.

Author Contributions: Conceptualization, Y.R. and S.L.; methodology, Y.S. and Y.R.; software, Y.R.; validation, Z.L. and Y.R.; formal analysis, Y.R.; investigation, L.L.; resources, B.Z.; data curation, Y.H.; writing—original draft preparation, Y.S.; writing—review and editing, Y.S. and S.L.; visualization, M.X.; supervision, K.Y.; project administration, S.L.; funding acquisition, Z.L. All authors have read and agreed to the published version of the manuscript.

Funding: This research was funded by the Guangzhou Bureau of EHV Power Transmission Company Technology Project (Grant No. 0101002022030301SB00054).

Data Availability Statement: The data presented in this study are available on request from the corresponding authors, as the data are part of an ongoing research study.

Conflicts of Interest: The authors declare that they have no known competing financial interests or personal relationships that could have appeared to influence the work reported in this paper.

References

1. Wróblewski, W.; Kowalik, R.; Januszewski, M.; Kurek, K. A Fuzzy OLTC Controller: Applicability in the Transition Stage of the Energy System Transformation. *Energies* **2024**, *17*, 2716. [CrossRef]
2. Dabaghi-Zarandi, F.; Behjat, V.; Gauvin, M.; Picher, P.; Ezzaidi, H.; Fofana, I. Power Transformers OLTC Condition Monitoring Based on Feature Extraction from Vibro-Acoustic Signals: Main Peaks and Euclidean Distance. *Sensors* **2023**, *23*, 7020. [CrossRef] [PubMed]
3. Maataoui, Y.; Chekenbah, H.; Boutfarjoute, O.; Puig, V.; Lasri, R. A Coordinated Voltage Regulation Algorithm of a Power Distribution Grid with Multiple Photovoltaic Distributed Generators Based on Active Power Curtailment and On-Line Tap Changer. *Energies* **2023**, *16*, 5279. [CrossRef]
4. Dabaghi-Zarandi, F.; Behjat, V.; Gauvin, M.; Picher, P.; Ezzaidi, H.; Fofana, I. Using Deep Learning to Detect Anomalies in On-Load Tap Changer Based on Vibro-Acoustic Signal Features. *Energies* **2024**, *17*, 1665. [CrossRef]
5. Cichoń, A.; Włodarz, M. OLTC Fault detection Based on Acoustic Emission and Supported by Machine Learning. *Energies* **2024**, *17*, 220. [CrossRef]
6. Ismail, F.B.; Mazwan, M.; Al-Faiz, H.; Marsadek, M.; Hasini, H.; Al-Bazi, A.; Yang Ghazali, Y.Z. An Offline and Online Approach to the OLTC Condition Monitoring: A Review. *Energies* **2022**, *15*, 6435. [CrossRef]
7. Cai, Y.; Fang, R.; Peng, C.; Huang, W. Mechanical Fault Diagnosis of On-Load Tap Changers Based on ANHGA-VMD and Coupled Hidden Markov Model. *High Volt. Eng.* **2021**, *47*, 3949–3959. (In Chinese)
8. Yang, R.; Zhang, D.; Li, Z.; Yang, K.; Mo, S.; Li, L. Mechanical fault diagnostics of power transformer on-load tap changers using dynamic time warping. *IEEE Trans. Instrum. Meas.* **2019**, *68*, 3119–3127. [CrossRef]
9. Zhao, L.; Feng, Y.; Xie, R.; Xue, J.; Zhang, L.; Wang, Z. Amplitude-Frequency Feature Extraction Method for Transformer Vibration Signals Based on Cross Wavelet. *High Volt. Eng.* **2019**, *45*, 505–511. (In Chinese)
10. Zeng, Q.; Wang, F.; Zheng, Y.; He, W. Fault Identification of Transformer On-Load Tap Changers Based on Convolutional Neural Network. *Autom. Electr. Power Syst.* **2020**, *44*, 144–151. (In Chinese)

11. Wang, F.; Zeng, Q.; Zheng, Y.; Qian, Y. Mechanical Fault Diagnosis of On-Load Tap Changers Based on Bayes Estimation Phase Space Fusion and CM-SVDD. *Proc. CSEE* **2020**, *40*, 358–368+402. (In Chinese)
12. Hendriks, J.; Dumond, P. Exploring the Relationship between Preprocessing and Hyperparameter Tuning for Vibration-Based Machine Fault Diagnosis Using CNNs. *Vibration* **2021**, *4*, 284–309. [CrossRef]
13. Zhang, X.; Zhang, M.; Xiang, Z.; Mo, J. Research on diagnosis algorithm of mechanical equipment brake friction fault based on MCNN-SVM. *Measurement* **2021**, *186*, 110065. [CrossRef]
14. Li, J.; Sun, S.; Lin, T. Fault Diagnosis of Bearings under Variable Conditions Based on Local Maxima and Second-order Synchrosqueezing Transform. *Noise Vib. Control* **2023**, *43*, 110. (In Chinese)
15. Lu, J.; Wang, Z.; Liu, F. Rolling Bearing Variable Load Fault Diagnosis Based on STFT-ECA-ResNet18 Network Model. *Noise Vib. Control* **2024**, *44*, 122–128. (In Chinese)
16. Cheng, J.; Lin, C.; Lu, Q.; Yang, C.; Li, P.; Yu, P.; Ge, H. A Decision Fusion SWT-RF Method for Rolling Bearing Enhanced Diagnosis under Low-quality Data. *IEEE Trans. Instrum. Meas.* **2024**, *73*, 3509511.
17. Sresakoolchai, J.; Kaewunruen, S. Detection and Severity Evaluation of Combined Rail Defects Using Deep Learning. *Vibration* **2021**, *4*, 341–356. [CrossRef]
18. Tang, H.; Tang, Y.; Su, Y.; Feng, W.; Wang, B.; Chen, P.; Zuo, D. Feature extraction of multi-sensors for early bearing fault diagnosis using deep learning based on minimum unscented kalman filter. *Eng. Appl. Artif. Intell.* **2024**, *127*, 107138. [CrossRef]
19. Nunnari, G.; Calvari, S. Exploring Convolutional Neural Networks for the Thermal Image Classification of Volcanic Activity. *Geomatics* **2024**, *4*, 124–137. [CrossRef]
20. Xu, X.; Zhang, H.; Ran, Y.; Tan, Z. High-Precision Segmentation of Buildings with Small Sample Sizes Based on Transfer Learning and Multi-Scale Fusion. *Remote Sens.* **2023**, *15*, 2436. [CrossRef]
21. Ma, W.; Mu, H.; Liu, W.; Zeng, X. Reliability Evaluation Method for Initiating Explosive Device Output Performance Based on SMOTE-Bootstrap Method in Small Sample Sizes. In Proceedings of the 2023 5th International Conference on System Reliability and Safety Engineering (SRSE), Beijing, China, 20–23 October 2023; IEEE: Piscataway, NJ, USA, 2023; pp. 439–444.
22. Liu, S.; Chen, J.; He, S.; Xu, E.; Lv, H.; Zhou, Z. Intelligent fault diagnosis under small sample size conditions via Bidirectional InfoMax GAN with unsupervised representation learning. *Knowl.-Based Syst.* **2021**, *232*, 107488. [CrossRef]
23. Tang, H.H.; Zhang, K.; Wang, B.; Zu, X.J.; Li, Y.Y.; Feng, W.W.; Jiang, X.; Chen, P.; Li, Q.A. Early bearing fault diagnosis for imbalanced data in offshore wind turbine using improved deep learning based on scaled minimum unscented kalman filter. *Ocean. Eng.* **2024**, *300*, 117392. [CrossRef]
24. Li, M.; Dong, W.; Zhang, G.; Zu, X.-J.; Li, Y.-Y.; Feng, W.-W.; Jiang, X.; Chen, P.; Li, Q.-A. A fault diagnosis method based on multi-agent reinforcement learning for small sample data. In Proceedings of the Fourth International Conference on Mechanical Engineering, Intelligent Manufacturing and Automation Technology (MEMAT 2023), Guilin, China, 20–22 October 2023; SPIE: Bellingham, WA, USA, 2024; Volume 13082, pp. 135–140.
25. Zhao, X.; Wang, L.; Yang, M.; Chen, Y.; Xiang, J. A Novel Small Sample Fault Diagnosis Method for Rolling Bearings via Continuous Wavelet Transform and Siamese Neural Network. *IEEE Sens. J.* **2024**, *24*, 24988–24996. [CrossRef]
26. Sun, X.; Ding, H.; Li, N.; Dong, X.; Liao, Y.; Liu, Z.; Bai, X. Intelligent fault diagnosis of rolling bearings under small samples based on lightweight UNet with attention-fused residual block. *Meas. Sci. Technol.* **2024**, *35*, 075002. [CrossRef]
27. Kalatzis, D.; Spyratou, E.; Karnachoriti, M.; Kouri, M.A.; Orfanoudakis, S.; Koufopoulos, N.; Pouliakis, A.; Danias, N.; Seimenis, I.; Kontos, A.G.; et al. Advanced Raman Spectroscopy Based on Transfer Learning by Using a Convolutional Neural Network for Personalized Colorectal Cancer Diagnosis. *Optics* **2023**, *4*, 310–320. [CrossRef]
28. Taebi, A.; Mansy, H.A. Time-Frequency Distribution of Seismocardiographic Signals: A Comparative Study. *Bioengineering* **2017**, *4*, 32. [CrossRef]
29. Dequit, A.; Nafa, F. Advancing Early Detection of Breast Cancer: A User-Friendly Convolutional Neural Network Automation System. *BioMedInformatics* **2024**, *4*, 992–1005. [CrossRef]
30. Lala, H.; Karmakar, S. Detection and experimental validation of high impedance arc fault in distribution system using empirical mode decomposition. *IEEE Syst. J.* **2020**, *14*, 3494–3505. [CrossRef]

Disclaimer/Publisher's Note: The statements, opinions and data contained in all publications are solely those of the individual author(s) and contributor(s) and not of MDPI and/or the editor(s). MDPI and/or the editor(s) disclaim responsibility for any injury to people or property resulting from any ideas, methods, instructions or products referred to in the content.